Contrib Mineral Petrol (2015) 169:43
DOI 10.1007/s00410-015-1138-3

ORIGINAL PAPER

Crystal structure, thermal expansivity, and elasticity of OH-chondrodite: trends among dense hydrous magnesium silicates

Yu Ye[1,2] · Steven D. Jacobsen[3] · Zhu Mao[4] · Thomas S. Duffy[5] · Sarah M. Hirner[2] · Joseph R. Smyth[2]

Received: 14 September 2014 / Accepted: 3 April 2015 / Published online: 19 April 2015

Abstract We report the structure and thermoelastic properties of OH-chondrodite. The sample was synthesized at 12 GPa and 1523 K, coexisting with hydroxyl-clinohumite and hydrous olivine. The Fe content Fe/(Fe + Mg) is 1.1 mol%, and the monoclinic unit-cell parameters are as follows: $a = 4.7459(2)$ Å, $b = 10.3480(7)$ Å, $c = 7.9002(6)$ Å, $\alpha = 108.702(7)°$, and $V = 367.50(4)$ Å^3. At ambient conditions, the crystal structure was refined in space group $P2_1/b$ from 1915 unique reflection intensities measured by single-crystal X-ray diffraction. The volume thermal expansion coefficient was measured between 150 and 800 K, resulting in $\alpha_V = 2.8(5) \times 10^{-9}$ (K^{-2}) $\times T + 40.9(7) \times 10^{-6}$ (K^{-1}) $- 0.81(3)$ (K)/T^2, with an average value of $38.0(9) \times 10^{-6}$ (K^{-1}). Brillouin spectroscopy was used to measure a set of acoustic velocities from which all 13 components (C_{ij}) of the elastic tensor were determined. The Voigt–Reuss–Hill average of the moduli yields for the adiabatic bulk modulus, $K_{S0} = 117.9(12)$ GPa, and for shear modulus, $G_0 = 70.1(5)$ GPa. The Reuss bound on the isothermal bulk modulus (K_{T0}) is 114.2(14) GPa. From the measured thermodynamic properties, the Grüneisen parameter (γ) is calculated to be 1.66(4). Fitting previous static compression data using our independently measured bulk modulus (isothermal Reuss bound) as a fixed parameter, we refined the first pressure derivative of the bulk modulus, $K_T' = 5.5(1)$. Systematic trends between H_2O content and physical properties are evaluated among dense hydrous magnesium silicate phases along the forsterite–brucite join.

Keywords Chondrodite · Dense hydrous magnesium silicates · Crystal structure · Thermal expansivity · Bulk modulus · Grüneisen parameter

Communicated by Timothy L. Grove.

Electronic supplementary material The online version of this article (doi:10.1007/s00410-015-1138-3) contains supplementary material, which is available to authorized users.

✉ Yu Ye
zylzylyeyu@gmail.com

[1] State Key Laboratory of Geological Processes and Mineral Resources, China University of Geosciences, Wuhan 430074, Hubei, People's Republic of China

[2] Department of Geological Sciences, University of Colorado, Boulder, CO 80309, USA

[3] Department of Earth and Planetary Sciences, Northwestern University, Evanston, IL 60208, USA

[4] School of Earth and Space Sciences, University of Science and Technology of China, Hefei 230026, Anhui, People's Republic of China

[5] Department of Geosciences, Princeton University, Princeton, NJ 08544, USA

Introduction

The dense hydrous magnesium silicate (DHMS) minerals along the brucite–forsterite join include phase A, norbergite, chondrodite, humite, and clinohumite (Fig. 1) as well as other DHMS minerals in the peridotite system. Among these phases, phase A, chondrodite, and clinohumite have been observed as dehydration products of serpentine as well as in experiments on MgO–SiO_2–H_2O systems at pressures of 5–12 GPa (Berry and James 2001; Smyth et al. 2006; Wunder 1998). These phases could serve as H_2O carriers in the Earth's upper mantle and transition zone. Due to the critical role of water in controlling silicate phase relations and physical properties at upper mantle conditions, the crystal structures and physical properties of DHMS have been

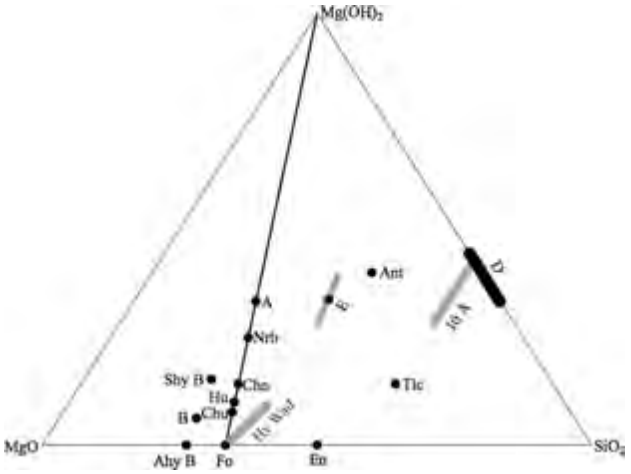

Fig. 1 Composition of hydrous magnesium silicates in the hydrous peridotite system ($MgO–SiO_2–Mg(OH)_2$). A: phase A; Nrb: norbergite; Chn: chondrodite; Hu: humite; Chu: clinohumite; Fo: forsterite; En: enstatite; B: phase B; Ahy B: anhydrous phase B; Shy B: supper hydrous phase B; Tlc: talc; Ant: antigorite; E: phase E (non-stoichiometric, Si/Mg 1.8–2.1, C_{H2O} 6–18 wt%); D: phase D (Si/Mg 0.5–0.8, C_{H2O} 13–19 wt%); 10 Å (C_{H2O} 7–13 wt%); Hy Wad: hydrous wadsleyite (C_{H2O} up to 3.3 wt%)

Table 1 Thermoelastic properties of phase A, chondrodite, and clinohumite (F-free) at ambient conditions

	Phase A	Chondrodite	Clinohumite
Formula	$Mg_7Si_2O_{14}H_6$	$Mg_5Si_2O_{10}H_2$	$Mg_9Si_4O_{18}H_2$
C_{H2O} (wt%)	11.8	5.4	2.9
ρ (g/cm^3)	2.949(1)[a]	3.099(1)[b]	3.134(1)[c]
α_0 (10^{-6} K^{-1})	46(2)[d]	38.0(9)[b]	36.8(6)[c]
K_{S0} (GPa)	100(1)[e]	118(1)[b]	119(2)[e]
G_0 (GPa)	61(1)[e]	70.1(5)[b]	77(1)[e]
V_P (km/s)	7.84(8)[e]	8.26(8)[b]	8.41(9)[e]
V_S (km/s)	4.55(7)[e]	4.76(4)[b]	4.96(8)[e]
K_{T0} (GPa)	97.5(4)[a]	114(1)[b]	119.4(7)[f]
K_T'	6.0(1)[a]	5.5(1)[f]	4.8(2)[f]
C_P (J kg^{-1} K^{-1})	924(1)[g]	874(1)[g]	884(1)[h]
Θ_{ac} (K)[i]	726(13)	741(10)	760(15)
γ^i	1.69(8)	1.66(4)	1.50(4)

[a] Crichton and Ross (2002); [b] this study; [c] Ye et al. (2013); [d] Pawley et al. (1995); [e] Phan (2009); [f] refined on the data from Ross and Crichton (2001) and Kuribayashi et al. (2004); [g] Cynn et al. (1996); [h] Holland and Powell 1998; [i] the Debye temperatures and Grüneisen parameters are calculated in this study

extensively studied (e.g., Angel et al. 2001; McGetchin et al. 1970; Kanzaki 1991; Faust and Knittle 1994; Irifune et al. 1998; Kawamoto 2006; Komabayashi and Omori 2006; Ohtani et al. 2000; Sanchez-Valle et al. 2006; Shieh et al. 2000; Wunder et al. 1995; Ye et al. 2013). The composition and various thermoelastic properties of phase A, chondrodite, and clinohumite are summarized in Table 1.

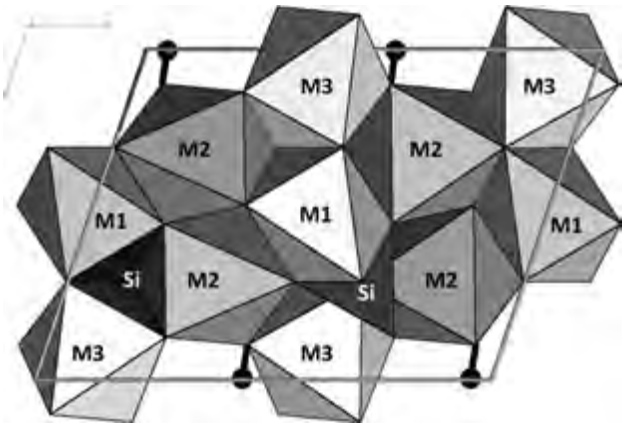

Fig. 2 Crystal structure of OH-chondrodite viewed down the *a*-axis, with hydrogen positions shown as black spheres. M1–M3 refer to (Mg, Fe) octahedra, and the silicate tetrahedron is labeled Si

The humite minerals are found in metamorphosed limestones and dolomites and contain variable proportions of F and OH (Friedrich et al. 2002). Variable Ti and F/OH humites are also known in high-pressure ultramafic rocks (Evans and Trommsdorff 1983) as well as being recently described in a serpentinized wehrlite (Shen et al. 2014). Within kimberlites, mineral associations including humites have indicated equilibrium pressures in excess of 6 GPa (Taskaev and Ilupin 1990). Synthetic hydroxyl-chondrodite (nominally $Mg_5Si_2O_{10}H_2$) is stable up to at least 12 GPa at temperatures below 1473 K (Burnley and Navrotsky 1996), and Fe–Ti-bearing compositions bracket the stability fields of chondrodite and clinohumite in typical mantle compositions (Khodyrev et al. 1992). Fluorine may significantly increase its thermal stability (Engi and Lindsley 1980) and incompressibility (Friedrich et al. 2002), but the estimated concentration of fluorine in the upper mantle is limited (e.g., McDonough and Sun 1995). Hence, the geological occurrence of chondrodite may be restricted to low-temperature regimes such as cold, subducting slabs, and the mantle wedge above them.

The crystal structure of chondrodite is illustrated in Fig. 2. The structure is monoclinic (space group $P2_1/b$, *a*-unique). The non-conventional setting of space group $P2_1/c$ can be chosen to preserve the association with the *a*- and *b*-axes of olivine. In the crystal structure of OH-chondrodite, there are three distinct (Mg,Fe)–O_6 octahedra (M1, M2, and M3) and one Si–O_4 tetrahedron (Si). The ratio of M1:M2:M3:Si equals 1:2:2:2, since the M1 sites are fixed at the special position of (1/2, 0, 1/2). Hydrogen atoms are bonded to O5 sites, which are also the positions for F anions in natural F-bearing samples. Thermoelastic properties of DHMS phases along the olivine–brucite join have been reported for a range of compositions (with variable H_2O, Fe, Ti, F, etc.) including thermal expansivity (Pawley et al. 1995; Ye et al. 2013, etc.), isothermal compressibility

(Crichton and Ross 2002; Kuribayashi et al. 2004; Friedrich et al. 2002; Holl et al. 2006; Ross and Crichton 2001), and adiabatic elastic moduli (Fritzel and Bass 1997; Jacobsen et al. 2008; Jiang et al. 2006; Sanchez-Valle et al. 2006; Sinogeikin and Bass 1999; Phan 2009; Xia et al. 1998). In this study, we examined the crystal structure of a Fe-bearing, OH-chondrodite sample by single-crystal X-ray diffraction and determined the lattice coefficients of thermal expansivity between 150 and 800 K. Brillouin spectroscopy was used to measure a set of velocities from three different platelets that constrain the thirteen independent C_{ij} of the elasticity tensor. By comparing the current results with physical properties of other DHMS phases along the forsterite–brucite join, we establish trends as a function water content that can be used to model the physical properties of mineral assemblages found in hydrated subducting slabs.

Experiments

Sample synthesis and composition

The Fe-bearing OH-chondrodite crystals were synthesized in the 5000-ton multi-anvil press at Bayerisches Geoinstitut, Bayreuth, Germany, run SZ0407B (Smyth et al. 2006). An outer 3.5-mm welded Pt capsule contained two separate 1.6-mm-diameter welded Pt inner capsules in a matrix of brucite to maintain H activity. The inner capsule contained a 1-mm single-crystal cube of San Carlos olivine, plus a mixture of brucite and forsterite. The inner capsules also contained small amount of a Re–ReO_2 oxygen buffer to maintain the iron in the ferrous state. The run was made in an 18-mm sintered MgO octahedron using 54-mm WC cubes with 8-mm corner truncations. The nominal pressure was 12 GPa at 1250 °C with a heating duration of 180 min. The original objective of the experiment was to hydrate the San Carlos olivine, but rupture of the inner capsule exposed the San Carlos olivine to excess brucite, with which it reacted to form phase A, chondrodite, and clinohumite. The chondrodite crystals were up to 0.25 mm in diameter and light tan in color.

A single crystal about 120 μm in size was selected and polished for chemical analysis by electron microprobe following the experimental procedure described previously for the coexisting clinohumite (Ye et al. 2013). Six points at different locations of the crystal were chosen for analysis, and the average values together with their standard deviations are listed in Table 2. The water content was calculated to be 5.26 wt%, assuming the molar ratio of H:O to be 2:10. The formula is expressed as $Mg_{5.047(4)}Fe_{0.058(2)}Ti_{0.0001}Mn_{0.0004(1)}Ni_{0.0018(5)}Al_{0.0017(2)}Ca_{0.0008(2)}Si_{1.945(3)}O_{10}H_2$, and Fe mol% = Fe/(Fe + Mg) = 1.1 % which is lower than those of the coexisting OH-clinohumite (4 % Fe) (Ye et al. 2013) and hydrous olivine (3 % Fe) (Jacobsen et al. 2008, hy-Fo_{97}) in the run products.

Single-crystal X-ray diffraction (XRD)

A single crystal of OH-chondrodite measuring 100 × 85 × 80 μm^3 was chosen for X-ray diffraction at ambient conditions. Unit-cell parameters were refined on a Bruker P4 four-circle diffractometer with a dual-scintillation point detector system using an 18-kW rotating Mo-anode X-ray source operating at 50 kV and 250 mA. The average wavelength for Mo$K\alpha_1$–$K\alpha_2$ mixed characteristic wavelengths was determined to be 0.71073 Å by measuring a spherical single crystal of anhydrous forsterite (Fo_{100}). Least squares fitting was performed on 48 centered reflections within the following classes: (120), (1$\bar{1}$2), (1$\bar{2}$2), (1$\bar{3}$1), (130), (11$\bar{2}$), (1$\bar{3}$2), (131), (210), (1$\bar{1}$3), (1$\bar{2}$3), (122), (1$\bar{4}$1), (211), (2$\bar{1}$2), (2$\bar{2}$3), (222), and (2$\bar{4}$1), and the refined unit-cell parameters at ambient condition are as follows: a = 4.7459(2) Å, b = 10.3480(7) Å, c = 7.9002(6) Å, α = 108.702(7)°, and V = 367.50(4) $Å^3$. Intensity data were collected using a Bruker APEX II CCD detector mounted on a P4 diffractometer up to 2θ = 75°. Refinement of atomic positions and anisotropic displacement parameters was carried out using SHELXL-97 (Sheldrick 2008) in the software package WinGX (Farrugia 2012), with the default neutral atom scattering factors in SHELXL-97. In total, 10,333 reflections were collected with 1915 unique and 1833 with $I > 4\sigma$ used

Table 2 Composition of OH-chondrodite SZ0407B from electron microprobe analyses

	wt%		apfu[a]		wt%		apfu
SiO_2	34.09(6)	Si	1.945(3)	NiO	0.04(1)	Ni	0.0018(5)
TiO_2	0.003(3)	Ti	0.0001(1)	MnO	0.008(3)	Mn	0.0004(1)
Al_2O_3	0.026(3)	Al	0.0017(2)	CaO	0.014(3)	Ca	0.0008(2)
MgO	59.34(5)	Mg	5.047(4)	H_2O[b]	5.26	H	2
FeO	1.22(3)	Fe	0.058(2)	Total	100.00(6)		

[a] Atoms per formula unit

[b] The wt% and apfu values for H_2O/H are calculated from stoichiometry, assuming that the molar ratio of H:O is 2:10

Table 3 Atomic positions and occupancy factors from X-ray intensity scan (space group: $P2_1/b$)

Atom	*x/a*	*y/b*	*z/c*	Occupancy
M1	0.5	0	0.5	Mg: 0.991(2)/ Fe: 0.009(2)
M2	0.00761(6)	0.17542(3)	0.30892(4)	Mg: 0.992(2)/ Fe: 0.008(2)
M3	0.48780(6)	0.88398(3)	0.07707(4)	Mg: 0.989(2)/ Fe: 0.011(2)
Si	0.07769(4)	0.14073(2)	0.70194(2)	0.983(2)
O1	0.77577(11)	0.00294(5)	0.29661(7)	1
O2	0.72759(11)	0.24411(5)	0.12853(7)	1
O3	0.22561(11)	0.16797(5)	0.52799(7)	1
O4	0.26251(11)	0.85683(5)	0.29738(7)	1
O5	0.26372(14)	0.06017(6)	0.10540(9)	1
H	0.109(3)	0.046(2)	0.004(3)	1

in the refinement. Model fit parameters are as follows: $R_1 = 0.0213$ for $I > 4\sigma$, and 0.0223 for all the unique reflections; goodness of fit (GooF) = 1.674; and for merging of equivalent reflections, $R_{int} = 0.039$.

The refined atomic position coordinates and occupancy factors are listed in Table 3, and the anisotropic displacement parameters are given in "Appendix 1". In this study, Fe and Mg occupancies in the M1, M2, and M3 sites were refined, as well as Si occupancy, and the O occupancies were fixed at full occupancy. In addition, the H position was refined with an isotropic displacement parameter (U_{eq}) fixed at 0.054.

The same single crystal of OH-chondrodite was then used for thermal expansion measurements below and above room temperature. At each temperature step, the refinement of unit-cell parameters was performed using the same experimental procedure as the room-temperature measurement described above. Low-temperature measurements were taken at 253, 203, and 153 K. Temperatures were measured and controlled by a Bruker LT-2A controller and N_2 gas stream nozzle. For high-temperature measurements, the crystal was transferred to a silica glass capillary, sealed at both ends. Ten high-temperature steps were carried out from 350 to 787 K using a Bruker high-temperature device with a two-prong ceramic-coated Pt wire radiant heater and an Omega temperature control unit (Ye et al. 2009). The refined unit-cell parameters at low and high temperatures are given in "Appendix 2".

Brillouin spectroscopy

Three crystals of OH-chondrodite (from run SZ0407B) were prepared for Brillouin scattering experiments by double-sided polishing to produce parallel plates measuring about 100 μm across and 30–50 μm thick. Polishing was carried out with 3-μm diamond lapping film and finishing with 1 μm and then finally 0.5-μm diamond lapping film to produce an optical-quality surface free of visible scratches.

Prior to Brillouin spectroscopy, Raman spectroscopy was carried out on each of the three platelets. Unpolarized Raman spectra were obtained using a 200-mW Ar-ion laser ($\lambda = 514.532$ nm) with a confocal optical setup in backscattering geometry using holographic optics and a single-grating 0.5-m spectrometer with a 1100 × 330 pixel CCD camera. Raman spectra of the three OH-chondrodite crystals used in the Brillouin scattering experiments are shown in Fig. 3a–d.

Brillouin spectra were obtained in a forward symmetric scattering geometry (Speziale and Duffy 2002; Speziale et al. 2014) with a six-pass Sandercock tandem Fabry–Perot interferometer, using a solid-state laser ($\lambda = 532.15$ nm, 150 mW at the sample). Acoustic velocities (V_i) were determined as:

$$V_i = \frac{\Delta\omega_i \lambda}{2\sin\left(\frac{\theta}{2}\right)}, \quad (1)$$

where $\Delta\omega_i$ is the Brillouin scattering frequency shift of the acoustic modes, and θ is the scattering angle in the sample (70° in this study). For each platelet, measurements were taken in ~5–10° steps with the total number of spectra in a given platelet depending on its size and the quality of the signal. Measured acoustic velocities are plotted as functions of azimuthal angle in Fig. 4a–c. Further details about the Brillouin scattering measurements can be found in Speziale and Duffy (2002) and Speziale et al. (2014).

Three platelets were used for Brillouin scattering, with the orientation of each platelet defined with three Eulerian angles (θ, ϕ, and χ). Chondrodite has a monoclinic structure with thirteen elastic constants: C_{11}, C_{22}, C_{33}, C_{44}, C_{55}, C_{66}, C_{12}, C_{13}, C_{23}, C_{15}, C_{25}, C_{35}, and C_{46}. The elastic constants and acoustic velocities are related by Christoffel's equation (Every 1980):

$$\det|C_{ijkl}n_j n_l - \rho V_{P,S}^2 \delta_{ik}| = 0 \quad (2)$$

where C_{ijkl} is the elastic tensor in full suffix notation, n_i is the direction cosine of the phonon propagation direction, density $\rho = 3.099$ g/cm^3 (according to the composition determined by EPMA and unit-cell volume from single-crystal XRD at ambient condition), and $V_{P,S}$ is the acoustic velocity of either longitudinal (V_P) or transverse (V_S) in the Brillouin spectra. The inversion was carried out by nonlinear least squares using Levenberg–Marquardt method (Press et al. 1988) with closed-form expressions for the Christoffel equation given

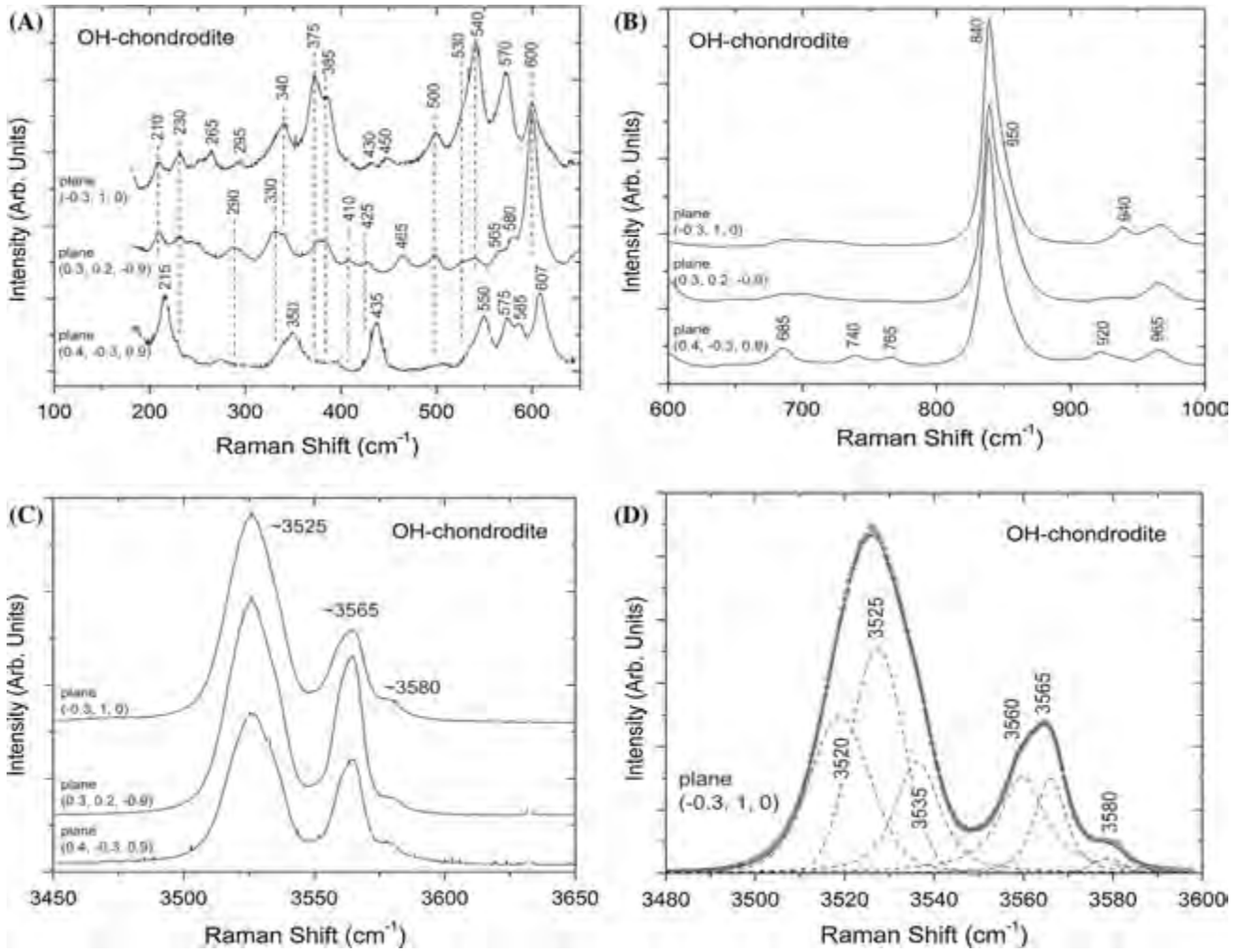

Fig. 3 Unpolarized Raman spectra of the three OH-chondrodite crystals used in the Brillouin scattering experiments: **a** low-wavenumber region, **b** mid-wavenumber region, **c** high-wavenumber region showing O–H stretching bands, **d** high-wavenumber region of one sample shown with the two main O–H stretching bands deconvolved into six different components (*dashed lines*), sum of the fitted peaks (*solid line*) and spectral data points (*gray dots*). The unpolarized Raman spectra were collected in backscatter geometry with the incident laser perpendicular to each plane expressed as (*hkl*), fitted by Brillouin spectroscopy

by Every (1980). The inversion process was iterative. The elastic constants of Sinogeikin and Bass (1999) were used as the initial model and held fixed, while the inversion was performed for the three Eulerian angles defining the orientation of each plane. The relationship between the Eulerian angles and the direction cosines of the phonon propagation direction is given by Shimizu (1995). In subsequent inversions, the elastic constants and orientations were alternately varied or allowed to vary together, and the process was continued until convergence was achieved. Different sets of initial elastic constants were tested to confirm that the final results were insensitive to the starting model. The results are shown in Fig. 4a–c. The good quality of the fit is demonstrated by the small root-mean-square difference between the measured and calculated velocities which was $V_{RMS} = 39$ m/s.

Results and discussion

Raman spectroscopy

Unpolarized Raman spectra of the three OH-chondrodite platelets used for Brillouin scattering are shown in Fig. 3. The spectra are generally similar to previous Raman studies of OH-chondrodite (Lin et al. 1999; Mernagh et al. 1999). In Fig. 3, the polished plane orientation is expressed as (*hkl*), fitted from the velocity dispersion curves in the Brillouin scattering study. Band assignments for some of the modes shown in Fig. 3 are given elsewhere (Cynn et al. 1996; Lin et al. 1999). In the O–H stretching region, we find a similar strong doublet as was found for F-free synthetic OH-chondrodite (Lin et al. 1999). The main band

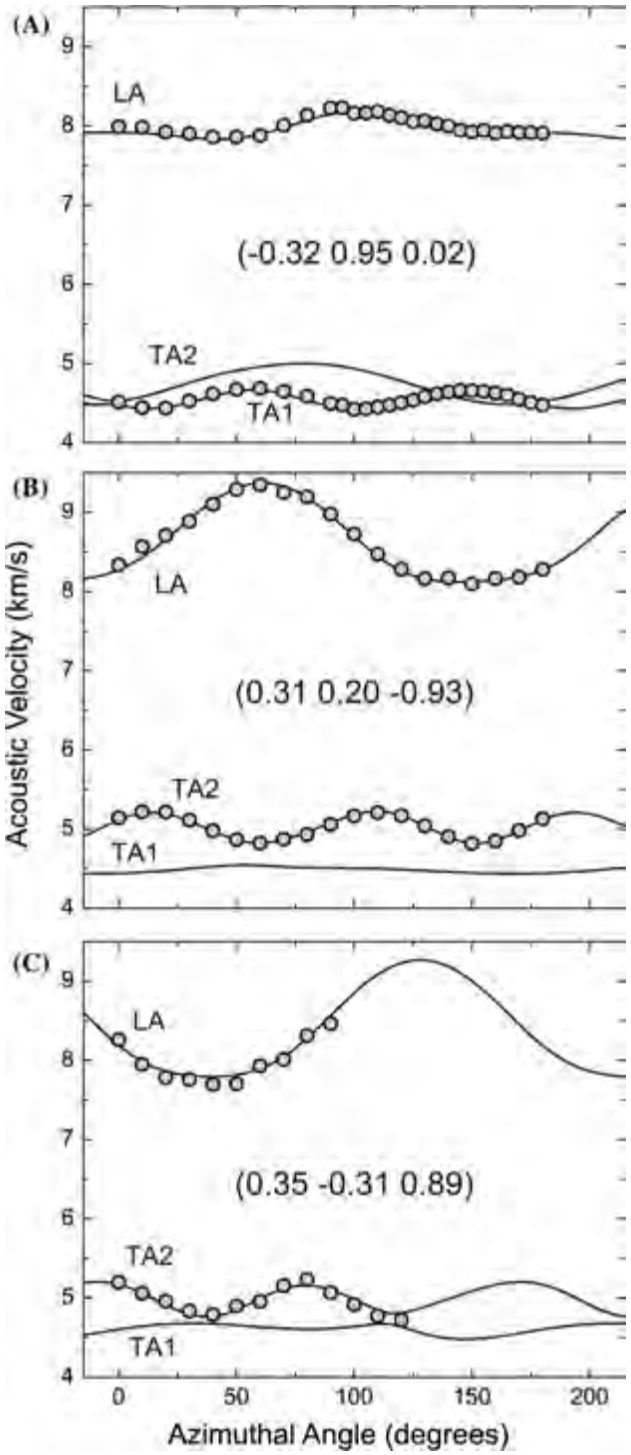

Fig. 4 **a–c** Longitudinal acoustic (LA) and transverse acoustic (TA) velocities in three different planes (*hkl*) of OH-chondrodite as a function of crystallographic direction. The azimuthal angle is relative to an arbitrary starting angle. The *solid curves* were calculated using the best-fit elastic constants for comparison with the measured velocities (*filled circles*)

positions shown in Fig. 3 are 3525 and 3565 cm^{-1}, which are shifted by about 10 cm^{-1} from the positions shown by Lin et al. (1999) at 3515 and 3554 cm^{-1}. Also in Fig. 3 is shown a deconvolution of the O–H stretching doublet (dashed lines), which is composed of at least four separate bands at 3525, 3560, 3565, and 3580 cm^{-1}. The 3525 cm^{-1} band may be further deconvolved into three separate bands to best fit the observed spectrum.

Crystal structure

According to the refined Mg and Fe occupancies in Table 3, the total Fe mol% is 0.9(4) %, consistent within uncertainty with that of (1.1 mol%) obtained from electron microprobe analyses. The Fe content from single-crystal XRD (site occupancy) is an approximation as minor elements (Ti, Ni, Mn, Ca, Al, < 0.04 mol%) were ignored in the structural refinement. The Si occupancy refinement from X-ray diffraction is consistent with that from microprobe analyses. The bond lengths and polyhedral volumes were calculated using the software package XTALDRAW (Downs et al. 1993) and listed in Table 4. The octahedral volumes show the order of M2 > M3 > M1, and the Si tetrahedral volume is 2.21(1) $Å^3$. The hydrogen bond geometry shows an O5–H distance of 1.06(2) Å and O5···H of 2.12(2) Å with a hydrogen bond angle of 122.7°. The O5–H bond length (O/F–H bonds in some chondrodites) has been refined by neutron diffraction (Friedrich et al. 2001 and Kunz et al. 2006), as well as X-ray diffraction (Ottolini et al. 2000 and Friedrich et al. 2002). Neutron diffraction better reflects the OF5–H interatomic distances than single-crystal X-ray diffraction. Friedrich et al. (2001) reported a bond length of 1.029(6) Å for OF–H and 1.872(6) Å for OF5···H, while Kunz et al. (2006) reported 0.976(7) and 1.940(7) Å, respectively. Our O5–H bond length is close to those from neutron experiments, whereas the O5···H interatomic distance is 10 % longer than previous results from neutron diffraction.

To compare the compositional effects of Fe, F, and Ti on the crystal structure of chondrodite, the unit-cell volumes and M–OF bond lengths are summarized in Table 5 for this study (SZ0407B) and literature values with the following abbreviations used throughout: Berry and James 2006, B02; Friedrich et al. 2001, 2002, F01 and F02; Fujino and Takéuchi 1978, F78; Gibbs et al. 1970, G70; Kuribayashi et al. 2004, K04; Kunz et al. 2006, K06; Ottolini et al. 2000, O00; Yamamoto 1977, Y77. The α angle in sample F78 is significantly larger than other samples in Table 5, which is likely due to the effect of Ti^{4+} incorporation

Table 4 Bond lengths (Å) and polyhedral volumes (Å^3)

M1		M2		M3	
O1 × 2	2.0805(5)	O1	2.0713(6)	O1	2.2413(6)
O3 × 2	2.1253(5)	O2	2.2257(6)	O2	2.0140(6)
O4 × 2	2.1227(5)	O3	2.0387(6)	O2	2.1123(6)
Avg. bond	2.1095(5)	O3	2.1772(6)	O4	2.1363(6)
Poly. V (Å^3)	12.04(1)	O4	2.1983(6)	O5	2.0604(7)
		O5	2.0630(7)	O5	2.0819(7)
		Avg. bond	2.1290(7)	Avg. bond	2.1077(7)
		Poly. V (Å^3):	12.47(1)	Poly. V (Å^3):	12.13(1)
Si				H	
O1		1.6461(6)		O5	1.06(2)
O2		1.6427(6)			
O3		1.6463(6)			
O4		1.6151(6)			
Avg. bond		1.6376(6)			
Poly. V (Å^3)		2.22(1)			

Table 5 Selected bond length (Å) for chondrodite samples from this and previous studies

	Fe%[a]	F%[b]	Ti%[a]	α (°)	V (Å^3)	M2-OF5	M3-OF5$_1$	M3-OF5$_2$
SZ0407B[c]	1.1	0	0	108.702(7)	367.50(4)	2.0628(5)	2.0599(6)	2.0825(6)
Y77[c]	0	0	0	108.71(5)	368.7(2)	2.133(3)	2.056(3)	2.091(3)
B02	1.4	77	0	109.11(1)	357.26(3)	2.054(8)	2.011(8)	2.015(9)
G70	1	65	0	109.059(2)	359.30(1)	2.045(2)	2.016(1)	2.042(2)
O00	0.8	62	0	109.08(2)	359.47(1)	2.051(3)	2.019(3)	2.045(3)
F01[d]	5.6	51	0.46	109.097(2)	363.14(4)	2.060(1)	2.033(1)	2.059(1)
F02[d]	5.6	58	0.46	109.065(1)	361.98(2)	2.057(8)	2.01(1)	2.055(9)
K06[d]	5.6	58	0.46	109.065(3)	361.98(2)	2.068(5)	2.048(5)	2.067(5)
K04[d]	4.4	37	0.4	109.07(1)	361.0(2)	2.057(1)	2.024(2)	2.053(1)
F78	12.5	0	8.4	109.33(1)	363.83(5)	2.051(2)	1.976(2)	1.987(2)

SZ0407B: this study; Y77: Yamamoto (1977); B02: Berry and James (2006); G70: Gibbs et al. (1970); O00: Ottolini et al. (2000); F01: Friedrich et al. (2001); F02: Friedrich et al. (2002); K06: Kunz et al. (2006); K04: Kuribayashi et al. (2004): F78: Fujino and Takéuchi (1978)

[a] Atomic percentage in the total metallic cations

[b] Molar ratio of F/(F + OH)

[c] Synthesized from experiments, while others are from natural sources

[d] Data measured at ambient condition

(Robinson et al. 1973). In addition, α angle values in SZ0407B and Y77 are 0.35–0.4° smaller than those in Y77, B02, G70, O00, F01, F02, K06, and K04, implying that F^- might increase the angle. The unit-cell volumes decrease in the order of SZ0407B and Y77 > F78 > F01, F02, K06 and K04 > B02 and G70 > Y77 consistent with the order of decreasing ionic radii (Fe^{2+} > Mg^{2+} > Ti^{4+}) and anions (O^{2-} > F^-). Samples SZ0407B, Y77, and F78 are F-free, while F78 has a high Ti^{4+} concentration of 8.4 mol%. Samples F01, F02, K06, and K04 have higher Fe^{2+} concentrations than B02, G70, and Y77, and B02 has the highest F^- content among these samples. The most significant effect of F^- on the crystal structure is that F^- decreases distances between OFOH and surrounding cations, i.e., one M2-OF bond and two M3-OFOH bonds. Samples SZ0407B and Y77 typically have larger M-OF bond lengths than other samples, as shown in Table 5, while sample F78 has significantly smaller M3-OF bond lengths, due to the occupancies of smaller cations Ti^{4+} in M3 site. Fe^{2+} should increase the M-O bond lengths, but such effect is not well observed here, perhaps because of the low concentration of Fe^{2+} in the reported crystal structures and, possible technical discrepancies among different measurements.

Table 6 Average thermal expansion coefficients for the unit-cell parameters and the principal expansion axes (153–787 K), and the orientations of the principal axes

Unit-cell parameters		Principal expansion axes		Orientations		
	α_0 (10^{-6} K^{-1})		α_0 (10^{-6} K^{-1})	a	b	c
a	12.7(3)	X_1	12.7(3)	1	0	0
b	11.5(2)	X_2	10.6(2)	0	0.8353	0.5499
c	14.6(4)	X_3	14.7(4)	0	−0.1636	0.9865
α	1.43(10)					
V	38.0(9)					

Thermal expansivity

To relate the anisotropy of thermal expansion to the crystal structure, the principal axes of thermal expansion are determined for this monoclinic structure, reducing the number of thermal expansion coefficients from 4 to 3: X_1, X_2, and X_3 (Cliffe and Goodwin 2012). The variations with temperature of the principle expansion axes are listed in "Appendix 2", and the average axial thermal expansion coefficients are listed in Table 6, as well as the orientations of the principle expansion axes. There is no difference between a and X_1 for a-unique monoclinic structure, while the thermal expansion coefficient of X_2 is 8 % smaller than that of b-axis for the compensation of α angle (>90°) expansion.

The thermal expansion coefficient is defined as:

$$\alpha(T) = \frac{1}{V}\left(\frac{\partial V}{\partial T}\right)_P = \left(\frac{\partial \ln(V)}{\partial T}\right)_P. \quad (3)$$

Fei (1995) proposed a useful formula for modeling $\alpha(T)$ above room temperature:

$$\alpha(T) = a_0 + a_1 T + \frac{a_2}{T^2} \quad \text{(Fei equation)}. \quad (4)$$

On the basis of the Mie-Grüneisen-Debye equation of state, Suzuki (1975), Suzuki et al. (1979), and Kumar (1995, 1996, 2003) developed expression for the unit-cell volume as function of temperature:

$$V_0(T) = V_0(0) \cdot \left[1 + \frac{1 - (1 - 4k \cdot E_{\text{th}}(T)/Q_0)^{1/2}}{2k}\right]$$
(Suzuki equation) (5)

$$V_0(T) = V_0(0) \cdot \left[1 - \frac{\ln[1 - (2k+2) \cdot E_{\text{th}}(T)/Q_0]^{1/2}}{2k+2}\right]$$
(Kumar equation) (6)

where $k = (K_T' - 1)/2 = 2.25$ ($K_T' = 5.5$ as in Table 1), $Q_0 = V_0(0)K_{T0}(0)/\gamma_{MGD}$. $V_0(0)$ and $K_{T0}(0)$ are the volume and isothermal bulk modulus taken at 0 K and 0 GPa. γ_{MGD} is a parameter related to the thermodynamic Grüneisen parameter γ_{th} (Barron et al. 1980). The thermal energy $E_{th}(T)$ is expressed by the Debye model:

$$E_{\text{th}}(T) = \frac{9nRT}{(\Theta_D/T)^3} \int_0^{\Theta_D/T} \frac{x^3}{e^x - 1} \cdot \mathrm{d}x \quad (7)$$

where R is the gas constant, n is the number of atoms in the formula unit (19 for OH-chondrodite), and Θ_D is the Debye temperature, and the acoustic Debye temperature Θ_{ac} is given by:

$$\Theta_{\text{ac}} = \frac{h}{k} \cdot \left(\frac{3N}{4\pi}\right)^{1/3} \cdot \left(\frac{n \cdot \rho}{M}\right)^{1/3} \cdot V_{\text{m}} \quad (8)$$

$$\frac{3}{V_{\text{m}}^3} = \frac{2}{V_{\text{s}}^3} + \frac{1}{V_{\text{p}}^3} \quad (9)$$

where h, k, N are Boltzmann, Plank, and Avogadro's constants, respectively, M is the molar mass, and V_m is the mean velocity. The calculated Θ_{ac} values for phase A, chondrodite, and clinohumite are listed in Table 1. The Θ_{ac} values for these DHMS phases are close to that (729 K) for San Carlos olivine (Liu and Li 2006), and we adopt $\Theta_D = 741$ K to calculate the thermal expansion coefficient of chondrodite in this study.

The unit-cell volume and principal expansion axes are plotted in Fig. 5a as a function of temperature and fitted by the curves calculated from Fei equation (Eq. 4). The principal expansion axes show an order of $\alpha_{X3} > \alpha_{X1} > \alpha_{X2}$. We derive the thermal expansion coefficients for unit-cell volume as follows: $a_0 = 40.9(7) \times 10^{-6}$ K^{-1}, $a_1 = 2.8(5) \times 10^{-9}$ K^{-2}, $a_2 = -0.81(3)$ K according to Fei equation. Next, the $V(T)$ dataset from this study is also fitted by Suzuki and Kumar equations (Eqs. 5, 6). We used K_{T0} (298 K) = 114 GPa (Table 1), and assuming that OH-chondrodite has the same dK_{T0}/dT as forsterite (−0.023 GPa/K, Kroll et al. 2012), we obtain K_{T0} (0 K) = 121 GPa. Then, the fittings result in $\gamma_{MGD} = 1.19(6)$ from Kumar equation; 1.21(8) from Suzuki equation; and V_0 (0 K) = 365.8(3) Å^3 from both Kumar and Suzuki equations.

The calculated α_V (T), calculated from Fei, Kumar, and Suzuki equations, are plotted in Fig. 5b, respectively, and extrapolated to 1500 K where the breakdown of OH-chondrodite was observed (Burnley and Navrotsky 1996). The

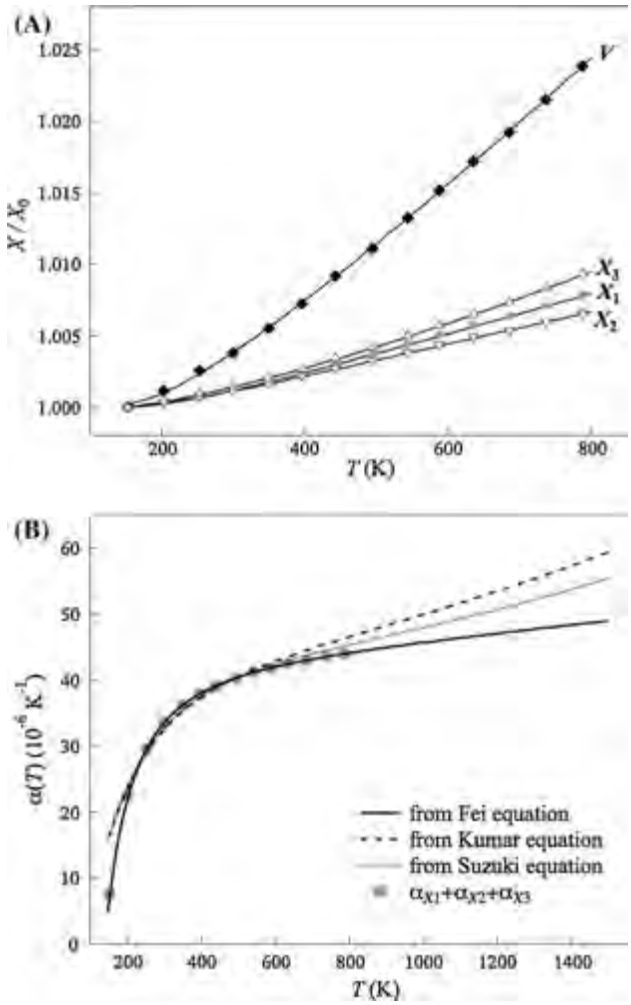

Fig. 5 **a** Unit-cell volume and principal expansion axes of OH-chondrodite as a function of temperature between 153 and 787 K. The *solid curves* are fitting to the data normalized to 153 K, using the Fei equation. Experimental uncertainties are smaller than the size of the symbols. **b** Volumetric thermal expansion coefficient as a function of temperature from Fei, Suzuki, and Kumar equations, which are extrapolated to 1500 K

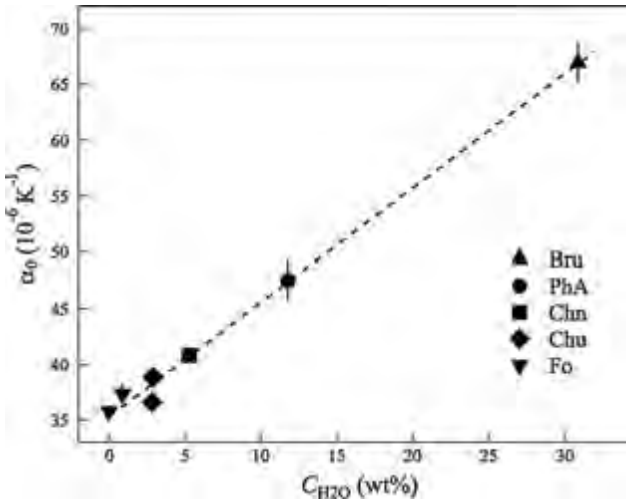

Fig. 6 Average thermal expansion coefficients as a function of water content for DHMS phases along the forsterite–brucite join. The temperature ranges are 300–787 K for forsterite (Fo, Ye et al. 2009), clinohumite (Chu, Ye et al. 2013), and chondrodite (Chn, this study); 293–873 K for phase A (PhA, Pawley et al. 1995); 299–593 K for brucite (Bru, Fukui et al. 2003)

Fei equation generates negative α_V below 140 K, whereas the Kumar and Suzuki equations give larger and more reasonable α_V at such low temperatures. From 200 to 800 K, these three equations agree with each other well, with discrepancy of 5 % at 800 K. When extrapolated to 1500 K, the Kumar and Suzuki equations indicate α_V values 20 and 13 % larger, respectively, compared with that from Fei equation. In addition, for α (T) relation as proposed by Fei (1995), the sum of the thermal expansion coefficients for principal axes at the measured temperatures is also plotted in Fig. 5b, which consistent with the solid curve of $\alpha_V(T)$ from Fei equation.

The axial thermal expansivity for the present Fe-bearing OH-chondrodite sample shows anisotropy in the order of $\alpha_c > \alpha_a > \alpha_b$, whereas axial compressibilities determined from single-crystal XRD data at high pressure yield an anisotropy of $\beta_b \approx \beta_c > \beta_a$ for Fe-free OH-chondrodite (Ross and Crichton 2001; Kuribayashi et al. 2004) and $\beta_b > \beta_c > \beta_a$ for Fe,F-bearing samples (Friedrich et al. 2002; Kuribayashi et al. 2004). The axial compressibilities are also consistent with the elasticity studies: $C_{11} > C_{33} \approx C_{22}$ for Fe-free OH-chondrodite (this study, in the following discussion) and $C_{11} > C_{33} > C_{22}$ for Fe,F-bearing sample (Sinogeikin and Bass 1999). Here, the elastic moduli are transferred to *a*-unique monoclinic symmetry to be consistent with the studies of crystal structure and isothermal compression. In this study, we find that the α angle increases with temperature, which is consistent with the observations that α decreases with pressure (Ross and Crichton 2001; Friedrich et al. 2002; Kuribayashi et al. 2004). The angle α increases as temperature increasing with a thermal expansion coefficient of $1.43(10) \times 10^{-6}$ K, consistent with that for clinohumite ($1.41–1.53 \times 10^{-6}$ K from Ye et al. 2013).

The average volume thermal expansion coefficients (α_0) for the DHMS phases along the forsterite–brucite join are plotted in Fig. 6, as a function of water content (C_{H2O}, expressed as wt% H_2O). The α_0 (V) values are recalculated over temperature range of 300–787 K for forsterite (Ye et al. 2009), clinohumite (Ye et al. 2013), and chondrodite (this study) to allow for consistent comparison with previous experiments on phase A (Pawley et al. 1995) and brucite (Fukui et al. 2003). There have been many previous studies on thermal expansivity of anhydrous forsterite (e.g., Ye et al. 2009; Kroll et al. 2012; and Trots et al. 2012). To simplify Fig. 6, we plotted the anhydrous forsterite thermal expansivity data from Ye et al. (2009) as representative. The α_0 for hydrous forsterite (0.89 wt% H_2O)

Table 7 Single-crystal elastic constants (in GPa) for chondrodite at ambient conditions

	This study	SB89		This study	SB89
Longitudinal			Off-diagonal		
$C_{11}(C_{33})$	188.0(7)	213.4(15)	$C_{12}(C_{13})$	61(10)	70(3)
$C_{22}(C_{11})$	278.0(10)	275.3(15)	$C_{13}(C_{23})$	71.4(7)	59(2)
$C_{33}(C_{22})$	195.7(7)	198.4(12)	$C_{23}(C_{12})$	74(3)	67(3)
Shear			$C_{15}(C_{14})$	3.9(4)	7.2(10)
$C_{44}(C_{66})$	64.0(10)	69.7(6)	$C_{25}(C_{24})$	2.6(10)	−1.7(12)
$C_{55}(C_{44})$	68.3(4)	72.1(9)	$C_{35}(C_{34})$	2.5(4)	−2.6(8)
$C_{66}(C_{55})$	71.3(5)	75.2(7)	$C_{46}(C_{56})$	4.1(6)	−0.7(4)

SB89: Sinogeikin and Bass (1999)

The elastic constants are given in the standard monoclinic coordinate system (*b*-unique, $P2_1/c$), while the values inside parentheses are those for an *a*-unique coordinate system ($P2_1/b$)

is ~0.8 × 10^{-6} K^{-1} larger than that for anhydrous forsterite. The Fe-bearing clinohumite (Fe% = 4.1 mol%) shows α_0 ~ 2.2 × 10^{-6} K^{-1} smaller than Fe-free clinohumite (Ye et al. 2013). The α_0 for the current OH-chondrodite sample is 40.8(4) × 10^{-6} K^{-1} in the range of 300–787 K, whereas it is 38.0(9) × 10^{-6} K^{-1} in 153–787 K.

A linear regression for the data of Fig. 6 yields a systematic relation between α_0 and C_{H2O} as:

$$\alpha_0\,(10^{-6}\mathrm{K}^{-1}) = 35.3(4) + 1.02(3) \times C_{H_2O}\,(\mathrm{wt\%}) \quad (R^2 = 0.9947) \tag{10}$$

Each additional 1 wt% H_2O content increases α_0 by 1.02(3) × 10^{-6} K^{-1} (or about 3 %). Thus, the thermal expansion coefficient increases with H_2O content for DHMS along the forsterite–brucite join, which is consistent with the observation that the bulk moduli decrease as H_2O content increases (Ross and Crichton 2001; Holl et al. 2006; Jacobsen et al. 2008; Sanchez-Valle et al. 2006).

After heating to 787 K, the single crystal of OH-chondrodite was quenched to room temperature, and the unit-cell parameters after heating are as follows: a = 4.7455(4) Å, b = 10.3475(8) Å, c = 7.9008(9) Å, α = 108.706(8)°, and V = 367.47(7) $Å^3$, consistent with the initial ones before heating. We conclude that this Fe-bearing OH-chondrodite sample persisted to 787 K at ambient pressure without any observable phase transition or dehydration.

Elastic moduli

The calculated elastic moduli for OH-chondrodite (Fe/(Mg + Fe) = 1.1 %) are listed in Table 7, in comparison with F-bearing chondrodite (Fe/(Mg + Fe) = 5.5 %, F/(F + OH) = 32 %, Sinogeikin and Bass 1999). Nearly all of the longitudinal and shear elastic constants are lower than those reported by Sinogeikin and Bass (1999) for a F-rich natural chondrodite. The Brillouin inversion was performed in standard monoclinic symmetry (*b*-unique, $P2_1/c$) where zigzag chains of edge-sharing octahedra are aligned along the *a*-axis and lie in the plane perpendicular to the *b*-axis. The elastic indices are also reported in the *a*-unique coordinate system ($P2_1/b$) (values given in parentheses in Table 7) to facilitate comparison with the studies of the crystal structure. The longitudinal constants C_{22} and C_{33} (in standard monoclinic symmetry hereafter) are close to the values from Sinogeikin and Bass (1999), whereas C_{11} is 12 % smaller. The shear constants C_{55} and C_{66} are about 5 % smaller, while C_{44} is 8 % smaller. The off-diagonal moduli are not

Table 8 Aggregate elastic moduli and pressure derivative of bulk modulus for chondrodite

	F/(F + OH)	Fe (mol%)	K_{T0} (GPa)	K_T'	G_0 (GPa)
This study	0	1.1	119.4[a]		71.1 (Voigt bound)
			116.4[a]		69.2 (Reuss bound)
			117.9(12)[a]		70.1(5) (VRH average)
			114.2[b]	5.5(1)[c]	
Sinogeikin and Bass (1999)	0.32	5.5	118.4(16)[a]		75.6(7)
Ross and Crichton (2001)	0	0	115.7(8)	4.9(2)	
Kuribayashi et al. (2004)	0	0	117(2)	4[d]	
Kuribayashi et al. (2004)	0.37	4.4	124.1(4)	4[d]	
Friedrich et al. (2002)	0.55	0	117(4)	5.6(1)	
Faust and Knittle (1994)	0.69	0	136.2	3.7[d]	

[a] Adiabatic bulk modulus

[b] K_{T0} calculated from Reuss bound K_{S0}

[c] Refined on the datasets of Ross and Crichton (2001) and Kuribayashi et al. (2004), with K_{T0} = 114.2 GPa

[d] Fixed without refinement

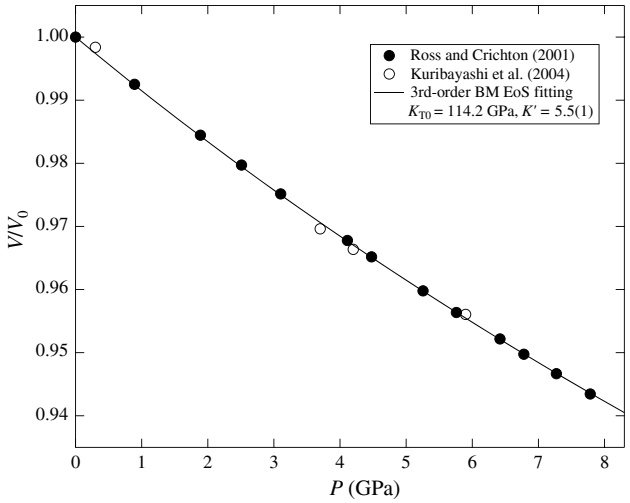

Fig. 7 Unit-cell volumes of Fe-free OH-chondrodite samples (Ross and Crichton 2001; Kuribayashi et al. 2008) as a function of pressure, with third-order Birch–Murnaghan equation of state (BM EoS) fitting. The volumes are normalized to their respective V_0 values at ambient conditions

constrained as well in either study. The Voigt–Reuss bounds and Voigt–Reuss–Hill (VRH) average of the aggregate moduli (Watt 1980) for OH-chondrodite are summarized in Table 8. The bulk modulus found here is identical within uncertainty to that obtained by Sinogeikin and Bass (1999) and consistent with those reported in static compression studies (Ross and Crichton, 2001, Kuribayashi et al., 2004; Friedrich et al., 2002). The shear modulus, G_0, is, however, about 6 % lower than that reported by Sinogeikin and Bass (1999) for a natural F-bearing sample, indicating that the shear modulus may increase with F content.

Using the density (ρ), isothermal bulk modulus (K_{S0}), thermal expansion coefficient (α_0), and heat capacity (C_P) listed in Table 1, we calculated the Grüneisen parameter (γ) for phase A, OH-chondrodite, and OH-clinohumite, from the formula:

$$\gamma = \frac{\alpha \cdot K_S}{\rho \cdot C_P} \tag{11}$$

The calculated γ values are also listed in Table 1. The Grüneisen parameter for phase A [1.69(8)], chondrodite [1.66(4)], and clinohumite [1.50(4)] is larger than that for forsterite (1.28, Gillet 1991), since phase A, chondrodite, and clinohumite have smaller C_P and ρ values than forsterite, whereas variation in the product $\alpha \cdot K_S$ is relatively less significant among these phases.

Because the Reuss bound on the bulk modulus, K_{S0}, corresponds to constant stress across grain boundaries, which is relevant for static compression studies, we calculate the isothermal Reuss bound bulk modulus for OH-chondrodite: K_{T0} = 114.2(14) GPa, with K_{S0} = 116.4(12) GPa and the formula:

Table 9 Studies of elasticity for DHMS along the olivine–brucite join, listed in the order of H_2O content increasing

	H_2O (wt%)	Density (g/cm^3)	Fe (mol%)	K_{S0} (GPa)	G_0 (GPa)	V_P (km/s)	V_S (km/s)
Olivine							
Suzuki et al. (1983)	0	3.225(1)	0	128.9(2)	81.4(2)	8.58(1)	5.02(1)
Zha et al. (1996)	0	3.221(1)	0	128.8(5)	81.6(2)	8.59(3)	5.03(1)
Webb (1989)	0	3.350(1)	10	129.5(2)	77.5(2)	8.34(1)	4.81(1)
Zha et al. (1998)	0	3.343(1)	10	131.1(19)	79.4(8)	8.42(9)	4.87(4)
Jacobsen et al. (2008, 2009)	0.8	3.240(1)	3	125.2(2)	77.7(1)	8.40(1)	4.90(1)
Jacobsen et al. (2008, 2009)	0.9	3.180(1)	0	125.4(4)	79.6(3)	8.53(2)	5.00(2)
Clinohumite							
Fritzel and Bass (1997)	2.0[a]	3.261(1)	6.5	125(2)	73(5)	8.26(9)	4.7(3)
Phan (2009)	2.9	3.134(1)	0	119(2)	77(1)	8.41(9)	4.96(8)
Chondrodite							
Sinogeikin and Bass (1999)	3.3[b]	3.227(1)	9.4	118(2)	75.6(7)	8.24(8)	4.84(5)
This study	5.3	3.099(1)	1.1	118(1)	70.6(5)	8.26(8)	4.76(4)
Phase A							
Sanchez-Valle et al. (2006)	11.7	2.976(1)	1.9	106(1)	61(1)	7.93(8)	4.53(8)
Phan (2009)	11.8	2.949(1)	0	100(2)	61(1)	7.84(9)	4.55(8)
Brucite							
Jiang et al. (2006)	30.9	2.380(1)	0	43.8(8)	35.2(3)	6.2(1)	3.85(3)
Xia et al. (1998)	30.9	2.380(1)	0	46(1)	34.9(5)	6.2(1)	3.83(5)

[a] F/(F + OH) = 0.29 for clinohumite

[b] F/(F + OH) = 0.32 for chondrodite

$$K_T = \frac{K_S}{1 + \alpha \cdot \gamma \cdot T} \quad (12)$$

Next, on the basis of reported compression datasets for Fe-free OH-chondrodite (Ross and Crichton 2001; Kuribayashi et al. 2004), we refined the pressure derivative of the bulk modulus, K_T' and obtain $K_T' = 5.5(1)$ (Fig. 7) by fixing K_{T0} at 114.2 GPa, the Reuss bound from Brillouin scattering. Figure 7 also shows that both these high-pressure datasets are consistent with each other. It should be noted that our OH-chondrodite has 1.1 mol% Fe, but such a low Fe concentration should probably be expected to have little effect on the bulk modulus. The refined results are also included in Table 8. Our results are consistent with the chondrodite sample from Friedrich et al. (2002) (Fe-free, F/(F + OH) = 0.32) which further indicates that F content does not strongly affect the bulk modulus. It should also be noted that the bulk modulus obtained by Faust and Knittle (1994) could be affected by non-hydrostatic stress due to their use of a methanol–ethanol–water pressure-transmitting medium at pressures up to 42 GPa.

Over the past three decades, extensive studies have been carried out on the elasticity of DHMS phases along the forsterite–brucite join (Suzuki et al. 1983; Webb 1989; Zha et al. 1996, 1998; Fritzel and Bass 1997; Sinogeikin and Bass 1999; Sanchez-Valle et al. 2006; Jacobsen et al. 2008, 2009; Phan 2009; as well as this study). The density (ρ), elastic moduli (K_{S0} and G_0, Voigt–Reuss–Hill averages), and acoustic velocities (V_P and V_S) are summarized in Fig. 8a, b, and c, respectively, with linear regression fittings listed below:

$$\rho(\mathrm{g/cm^3}) = 3.27(2) - 0.029(2) \times C_{H_2O} \quad (R^2 = 0.9767) \quad (13)$$

$$K_{S0}(\mathrm{GPa}) = 129.6(9) - 2.69(8) \times C_{H_2O} \quad (R^2 = 0.9898) \quad (14)$$

$$G_0(\mathrm{GPa}) = 79.3(6) - 1.45(5) \times C_{H_2O} \quad (R^2 = 0.9866) \quad (15)$$

$$V_P(\mathrm{km/s}) = 8.54(4) - 0.073(3) \times C_{H_2O} \quad (R^2 = 0.9724) \quad (16)$$

$$V_S(\mathrm{km/s}) = 4.95(3) - 0.036(2) \times C_{H_2O} \quad (R^2 = 0.9565) \quad (17)$$

The linear fits show that 1 wt% H_2O reduces K_{S0} and G_0 by 2.69(8) GPa (2 %) and 1.45(5) GPa (2 %), respectively, We also find that the isothermal bulk modulus (K_{T0}) decreases by 2.71 GPa for every 1 wt% H_2O added along the forsterite–brucite join (Ross and Crichton 2001; Holl et al. 2006). On the other hand, a linear relation for density versus water content is plotted in Fig. 8a. Addition of 1 wt% H_2O reduces ρ by 0.029(2) g/cm^3, and

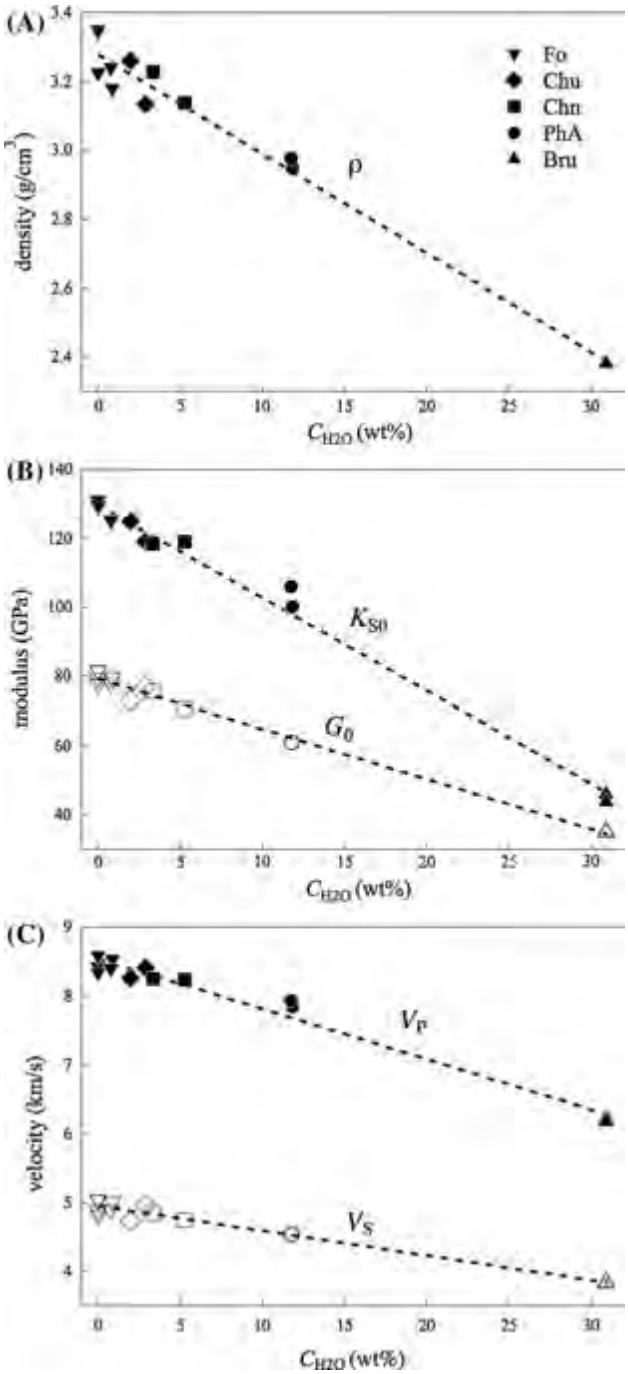

Fig. 8 Elastic properties of DHMS along the forsterite–brucite join: **a** density as a function water content, **b** bulk modulus (K_0) and shear modulus (G_0) as a function of water content, **c** compressional (V_P) and shear-wave (V_S) velocities as a function of water content. Linear fits to the data (*dashed lines*) are given in the text (Eqs. 13–17). References are given in Table 9

linear regressions for moduli and velocities versus density (Birch's law) could be fulfilled on the basis of Eq. (13).

In summary, we have presented new thermoelastic properties of OH-chondrodite, which was synthesized at 12 GPa and 1523 K, and coexists with OH-clinohumite and

hydrous olivine. The synthesis conditions correspond to the pressure–temperature condition around 360 km depth in a hydrous subducting slab. The chondrodite sample was characterized by multiple experimental methods: electron microbe, Raman spectroscopy, single-crystal X-ray diffraction (153–787 K), and finally Brillouin spectroscopy. For DHMS phases along the forsterite–brucite joint, every 1 wt% increase in C_{H2O} increases the mean thermal expansion coefficient (α_0) by 3 %, decreases the moduli (K_{T0}, K_{S0}, and G_0) by 2 %, and decreases the seismic velocities (V_P and V_S) by ~8 %. Hydration also enlarges the Grüneisen parameters for phase A, chondrodite, and clinohumite by 17–32 %, compared with anhydrous forsterite. The elastic properties of OH-chondrodite found in this study are consistent with the previous isothermal compression studies of Fe,F-free samples. The thermal expansion coefficient $\alpha(T)$ at ambient pressure is constrained by different models. The Fei equation yields: $\alpha_V = 2.8(5) \times 10^{-9}$ (K^{-2}) $\times T + 40.9(7) \times 10^{-6}$ (K^{-1}) – 0.81(3) (K)/T^2 (150–800 K); Suzuki and Kumar equations fit: V_0 (0 K) = 365.8(3) Å^3, Θ = 741 K, γ_{MGD} = 1.20(9) [γ = 1.66(4) calculated from Eq. 11]. The thermoelastic properties reported in this study are important to anchoring more complete *P–V–T* equations of state for chondrodite and other DHMS phases in future studies at simultaneous high pressure and high temperature.

Acknowledgments This work was supported by US NSF grants EAR-1452344 (SDJ), EAR-1113369 (JRS), and EAR-114854 (TSD). SDJ also acknowledges support from the Carnegie/DOE Alliance Center (CDAC), and the David and Lucile Packard Foundation. Synthesis was performed at Bayerisches Geoinstitut, University of Bayreuth, Germany, and supported in part by the Alexander von Humboldt Foundation.

Appendix 1

See Table 10.

Appendix 2

See Table 11.

Table 10 Anisotropic displacement parameters (Å^2)

Atom	U_{11}	U_{22}	U_{33}	U_{23}	U_{13}	U_{12}	U_{eq}
M1	0.0058(2)	0.0069(2)	0.0061(2)	0.0014(1)	0.0009(1)	0.0005(1)	0.0064(1)
M2	0.0085(2)	0.0065(2)	0.0071(2)	0.0029(1)	−0.0004(1)	0.0004(1)	0.0072(1)
M3	0.0072(1)	0.0094(2)	0.0074(1)	0.0040(1)	−0.0004(1)	0.0004(1)	0.0077(1)
Si	0.0042(1)	0.0056(1)	0.0054(1)	0.0022(1)	0.0000(0)	0.0000(0)	0.0050(1)
O1	0.0074(2)	0.0065(2)	0.0084(2)	0.0030(1)	0.0005(2)	−0.0001(1)	0.0073(1)
O2	0.0068(2)	0.0074(2)	0.0070(2)	0.0015(2)	0.0002(1)	−0.0001(1)	0.0073(1)
O3	0.0066(2)	0.0082(2)	0.0065(2)	0.0035(1)	0.0002(1)	−0.0001(1)	0.0068(1)
O4	0.0043(2)	0.0084(2)	0.0075(2)	0.0027(2)	0.0001(1)	0.0000(1)	0.0067(1)
O5	0.0189(3)	0.0100(2)	0.0202(3)	0.0080(2)	0.0127(2)	0.0059(2)	0.0156(1)
H							0.054 (fixed)

Table 11 Unit-cell parameters of chondrodite as functions of temperature, as well as the principle expansion axes, which are normalized to the ones at 153 K

T (K)	a (Å)	b (Å)	c (Å)	α (°)	V (Å^3)	X_1/X_{10}	X_2/X_{20}	X_3/X_{30}
153(2)	4.7402(3)	10.3341(8)	7.8899(8)	108.687(8)	366.12(4)	1	1	1
203(2)	4.7419(3)	10.3387(8)	7.8926(8)	108.693(8)	366.53(4)	1.00036	1.00030	1.00045
253(2)	4.7438(3)	10.3439(7)	7.8969(7)	108.698(7)	367.04(4)	1.00078	1.00076	1.00099
300(2)	4.7459(2)	10.3480(7)	7.9002(7)	108.702(7)	367.50(4)	1.00120	1.00114	1.00142
350(3)	4.7489(2)	10.3530(7)	7.9052(7)	108.706(8)	368.13(4)	1.00183	1.00164	1.00201
396(3)	4.7516(2)	10.3583(7)	7.9105(8)	108.708(9)	368.77(4)	1.00240	1.00217	1.00266
443(3)	4.7546(2)	10.3637(7)	7.9168(7)	108.715(9)	369.47(4)	1.00304	1.00267	1.00344
495(4)	4.7578(2)	10.3695(7)	7.9226(8)	108.722(9)	370.18(4)	1.00371	1.00318	1.00418
544(4)	4.7610(2)	10.3771(7)	7.9286(7)	108.735(9)	370.95(5)	1.00439	1.00380	1.00498
587(4)	4.7640(2)	10.3827(8)	7.9345(8)	108.737(8)	371.67(5)	1.00502	1.00435	1.00571
635(5)	4.7674(3)	10.3892(8)	7.9403(9)	108.750(9)	372.41(6)	1.00574	1.00486	1.00648
685(5)	4.7704(3)	10.3951(8)	7.9470(9)	108.764(9)	373.14(6)	1.00637	1.00534	1.00734
736(6)	4.7738(3)	10.4022(8)	7.9545(9)	108.771(9)	373.99(6)	1.00709	1.00599	1.00829
787(6)	4.7773(3)	10.4099(8)	7.9619(9)	108.795(9)	374.84(6)	1.00783	1.00653	1.00929

References

Angel RJ, Frost DJ, Ross NL, Hemley RJ (2001) Stabilities and equations of state of dense hydrous magnesium silicates. Phys Earth Planet Int 127:181–196

Barron THK, Collins JG, White GK (1980) Thermal expansion of solids at low temperatures. Adv Phys 29:609–730

Berry AJ, James M (2001) Refinement of hydrogen positions in synthetic hydroxyl-clinohumite by powder neutron diffraction. Am Mineral 86:181–184

Berry AJ, James M (2006) Refinement of hydrogen positions in natural chondrodite by powder neutron diffraction: implications for the stability of humite minerals. Miner Mag 66:441–449

Burnley PC, Navrotsky A (1996) Synthesis of high-pressure hydrous magnesium silicates: observations and analysis. Am Mineral 81:317–326

Cliffe MJ, Goodwin AL (2012) PASCal: a principal-axis strain calculator for thermal expansion and compressibility for thermal expansion and compressibility determination. J Appl Crystallogr 45:1321–1329

Crichton WA, Ross NL (2002) Equation of state of dense hydrous magnesium silicate Phase A, $Mg_7Si_2O_8(OH)_6$. Am Mineral 87:333–338

Cynn H, Hofmeister AM, Burney PC, Navrotsky A (1996) Thermodynamic properties and hydrogen speciation from vibrational spectra of dense hydrous magnesium silicates. Phys Chem Miner 23:361–376

Downs RT, Bartelmehs KL, Gibbs GV, Boisen MB (1993) Interactive software for calculating and displaying X-ray or neutron powder diffractometer patterns of crystalline materials. Am Mineral 78:1104–1107

Engi M, Lindsley DH (1980) Stability of titanian clinohumite: experiments and thermodynamic analysis. Contrib Mineral Petrol 72:1935–1938

Evans BW, Trommsdorff V (1983) Fluorine hydroxyl titanian clinohumite in alpine recrystallized garnet peridotite: compositional controls and petrologic significance. Am J Sci 283:355–369

Every AG (1980) General closed-form expressions for acoustic waves in elastically anisotropic solids. Phys Rev B 22:1746–1760

Farrugia LJ (2012) WinGX and ORTEP for Windows:an update. J Appl Cryst 45:849–854

Faust J, Knittle E (1994) Static compression of chondrodite: implications for water in the upper mantle 21. Geophys Res Lett 21(18):1935–1938

Fei Y (1995) Thermal expansion. In: Ahrens JT (ed) Mineral physics and crystallography, vol 2. AGU Ref. Shelf, pp 29–44

Friedrich A, Lager GA, Kunz M, Chakoumakos BC, Smyth JR, Schultz AJ (2001) Temperature-dependent single-crystal neutron diffraction study of natural chondrodite and clinohumite. Am Mineral 86:981–989

Friedrich A, Lager GA, Ulmer P, Kunz M, Marshall WG (2002) High-pressure single-crystal X-ray and powder neutron study of F, OH/OD-chondrodite: compressibility, structure, and hydrogen bonding. Am Mineral 87:931–939

Fritzel TLB, Bass JD (1997) Sound velocities of clinohumite, and implications for water in Earth's upper mantle. Geophys Res Lett 24(9):1023–1026

Fujino K, Takéuchi Y (1978) Crystal chemistry of titanian chondrodite and titanian clinohumite of high-pressure origin. Am Mineral 63:535–543

Fukui T, Ohtaka O, Suziki T, Funakoshi K (2003) Thermal expansion of $Mg(OH)_2$ brucite under high pressure and pressure dependence of entropy. Phys Chem Miner 30:511–516

Gibbs GV, Ribbe PH, Anderson CP (1970) The crystal structure of the humite minerals. II. Chondrodite. Am Mineral 55:1182–1194

Gillet P (1991) High-temperature thermodynamic properties of forsterite. J Geophys Res 96(B7):11805–11816

Holl CM, Smyth JR, Manghnani MH, Amulele GM, Sekar M, Frost DJ, Prakapenka VB, Shen G (2006) Crystal structure and compression of an iron-bearing Phase A to 33 GPa. Phys Chem Miner 33:192–199

Holland TJB, Powell R (1998) An internally consistent thermodynamic data set for phases of petrological interest. J Metamorphic Geol 16:309–343

Irifune T, Kubo N, Isshiki M, Yamasaki Y (1998) Phase transformations in serpentine and transportation of water into the lower mantle. Geophys Res Lett 25(2):203–206

Jacobsen SD, Jiang F, Mao Z, Duffy TS, Smyth JR, Holl CM, Frost DJ (2008) Effects of hydration on the elastic properties of olivine. Geophys Res Lett 35:L14303

Jacobsen SD, Jiang F, Mao Z, Duffy TS, Smyth JR, Holl CM, Frost DJ (2009) Correction to "Effects of hydration on the elastic properties of olivine". Geophys Res Lett 36:L12302

Jiang F, Speziale S, Duffy TS (2006) Single-crystal elasticity of brucite, $Mg(OH)_2$, to 15 GPa by Brillouin scattering. Am Mineral 91:1893–1900

Kanzaki M (1991) Stability of hydrous magnesium silicate in the mantle transition zone. Phys Earth Planet Inter 66:307–312

Kawamoto T (2006) Hydrous phases and water transport in the subducting Slab. Reviews Mineral Geochem 62:273–289

Khodyrev OY, Agoshkow VM, Slutsky AB (1992) The system peridotite-aqueous fluid at upper mantle parameters. Trans Dokl USSR Acad Sci: Earth Sci Sect 312:255–258

Komabayashi T, Omori S (2006) Internally consistent thermodynamic data set for dense hydrous magnesium silicates up to 35 GPa, 1600 & #xB0;C: implications for water circulation in the Earth's deep mantle. Phys Earth Planet Int 156:89–107

Kroll H, Kirfel A, Heinemann R, Barbier B (2012) Volume thermal expansion and related thermophysical parameters in the Mg, Fe olivine solid-solution series. Eur J Mineral 24:935–956

Kumar M (1995) High pressure equation of state for solids. Phys B 212:391–394

Kumar M (1996) Application of high pressure equation of state for different classes of solids. Phys B 217:143–148

Kumar M (2003) Thermoelastic properties of minerals. Phys Chem Minerals 30:556–558

Kunz M, Lager GA, Burgi HB, Fernandez-Diaz MT (2006) High-temperature single-crystal neutron diffraction study of natural chondrodite. Phys Chem Miner 33:17–27

Kuribayashi T, Kagi H, Tanaka M, Akizuki M, Kudoh Y (2004) High-pressure single crystal X-ray diffraction and FT-IR observation of natural chondrodite and synthetic OH-chondrodite. J Miner Petrol Sci 99:118–129

Kuribayashi T, Tanaka M, Kudoh Y (2008) Synchrotron X-ray analysis of norbergite, $Mg_{2.98}Fe_{0.01}Ti_{0.02}Si_{0.99}O_4(OH_{0.31}F_{1.69})$ structure at high pressure up to 8.2 GPa. Phys Chem Miner 35:559–568

Lin C-C, Liu L-G, Irifune T (1999) High-pressure Raman spectroscopic study of chondrodite. Phys Chem Miner 26(3):226–233

Liu W, Li B (2006) Thermal equation of state of $(Mg_{0.9}Fe_{0.1})_2SiO_4$ olivine. Phys Earth Planet Int 157:188–195

McDonough WF, Sun S-S (1995) The composition of the Earth. Chem Geol 120:223–259

McGetchin TR, Silver LT, Chodos AA (1970) Titanoclinohumite: a possible mineralogical site for water in the upper mantle. J Geophys Res 75:255–259

Mernagh TP, Liu L-G, Lin C-C (1999) Raman spectra of chondrodite at various temperatures. J Raman Spect 30:963–969

Ohtani E, Mizobata H, Yurimoto H (2000) Stability of dense hydrous magnesium silicate phases in the systems Mg_2SiO_4–H_2O and $MgSiO_3$–H_2O at pressures up to 27 GPa. Phys Chem Miner 27:533–544

Ottolini L, Cámara F, Bigi S (2000) An investigation of matrix effects in the analysis of fluorine in humite-group minerals by EMPA, SIMS, and SREF. Am Mineral 85:89–102

Pawley AR, Redfern SAT, Wood BJ (1995) Thermal expansivities and compressibilites of hydrous phases in the system MgO–SiO_2–H_2O: talc, phase A and 10-Å phase. Contrib Mineral Petrol 122:301–307

Phan HT (2009) Elastic properties of hydrous phases in the deep mantle: high-pressure ultrasonic wave velocity measurements on clinohumite and Phase A (dissertation). ETH Zürich, No: 18091, p 125

Press WH, Flannery BP, Teukolsky SA, Vetterling WT (1988) Numerical recipes in C: the art of scientific computing. Cambridge University Press, Cambridge

Robinson K, Gibbs GV, Ribbe PH (1973) The crystal structure of the humite minerals IV. Clinohumite and titanoclinohumite. Am Mineral 58:43–49

Ross NL, Crichton WA (2001) Compression of synthetic hydroxyl-clinohumite [$Mg_9Si_4O_{16}(OH)_2$] and hydroxylchondrodite [$Mg_5Si_2O_8(OH)_2$]. Am Mineral 86:990–996

Sanchez-Valle C, Sinogeikin SV, Smyth JR, Bass JD (2006) Single-crystal elastic properties of dense hydrous magnesium silicate phase A. Am Mineral 91:961–964

Sheldrick GM (2008) A short history of SHELX. Acta Cryst. A. 64:112–122

Shen T, Hermann J, Zhang L, Padron-Navarta JA, Chen J (2014) FTIR spectroscopy of Ti-chondrodite, Ti–clinohumite, and olivine in deeply subducted serpentinites and implications for the deep water cycle. Contrib Mineral Petrol. doi:10.1007/s00410-014-0992-8

Shieh SR, Mao H-K, Hemley RJ, Ming LC (2000) In situ X-ray diffraction studies of dense hydrous magnesium silicates at mantle conditions. Earth Planet Sci Lett 177:69–80

Shimizu H (1995) High-pressure Brillouin scattering of molecular single-crystals grown in a diamond-anvil cell. In: Senoo M, Suito K, Kobayashi T, Kubota H (eds) High Press Res Solid. Elsevier, Netherlands, pp 1–17

Sinogeikin SV, Bass JD (1999) Single-crystal elastic properties of chondrodite: implications for water in the upper mantle. Phys Chem Miner 26:297–303

Smyth JR, Frost DJ, Nestola F, Holl CM, Bromiley C (2006) Olivine hydration in the deep upper mantle: effects of temperature and silica activity. Geophys Res Lett 33:L15301

Speziale S, Duffy TS (2002) Single-crystal elastic constants of fluorite (CaF_2) to 9.3 GPa. Phys Chem Miner 29:465–472

Speziale S, Marquardt H, Duffy TS (2014) Brillouin scattering and its application in geosciences. In: Henderson GS, Neuville DR, Downs RT (eds) Spectroscopic methods in mineralology and materials sciences, vol 78. Mineralogical Society America, Chantilly, pp 543–603

Suzuki I (1975) Thermal expansion of periclase and olivine, and their anharmonic properties. J Phys Earth 23:145–149

Suzuki I, Oajima S, Seya K (1979) Thermal expansion of single-crystal manganosite. J Phys Earth 27:63–69

Suzuki I, Anderson OL, Sumino Y (1983) Elastic properties of a single-crystal forsterite Mg_2SiO_4, up to 1200 K. Phys Chem Miner 10:38–46

Taskaev VI, Ilupin IP (1990) Association of clinohumite and K-richterite in the kimberlite of Kollektivnaya pipe. Doklady Akademii Natsional'naya USSR 310(3):683–686

Trots DM, Kurnosov A, Boffa Ballaran T, Frost DJ (2012) High-temperature structural behaviors of anhydrous wadsleyite and forsterite. Am Mineral 97:1582–1590

Watt JP (1980) HashinShtrikman bounds on the effective elastic moduli of polycrystals with monoclinic symmetry. J Appl Phys. doi:10.1063/1.327803

Webb SL (1989) The elasticity of the upper mantle orthosilicates olivine and garnet to 3 GPa. Phys Chem Miner 16:684–692

Wunder B (1998) Equilibrium experiments in the system MgO–SiO_2–H_2O (MSH): stability fields of clinohumite–OH [$Mg_9Si_4O_{16}(OH)_2$], chondrodite–OH [$Mg_5Si_2O_8(OH)_2$] and phase A [$Mg_7Si_2O_8(OH)_6$]. Contrib Mineral Petrol 132:111–120

Wunder B, Medenbach O, Daniels P, Schreyer W (1995) First synthesis of the hydroxyl end-member of humite, $Mg_2Si_3O_{12}(OH)_2$. Am Mineral 80:638–640

Xia X, Weidner DJ, Zhao H (1998) Equation of state of brucite: single-crystal Brillouin spectroscopy study and polycrystalline pressure–volume–temperature measurements. Am Mineral 83:68–74

Yamamoto K (1977) The crystal structure of hydroxyl-chondrodite. Acta Crystallogr B 33:1481–1485

Ye Y, Schwering RA, Smyth JR (2009) Effects of hydration on thermal expansion of forsterite, wadsleyite, and ringwoodite at ambient pressure. Am Mineral 94:899–904

Ye Y, Smyth JR, Jacobsen SD, Goujon C (2013) Crystal chemistry, thermal expansion, and Raman spectra of hydroxyl-clinohumite: implications for water in Earth's interior. Contrib Mineral Petrol 165:563–574

Zha C-S, Duffy TS, Downs RT, Mao H-K, Hemley RJ (1996) Sound velocity and elasticity of single-crystal forsterite to 16 GPa. J Geophys Res 101(B8):17535–17545

Zha C-S, Duffy TS, Downs RT, Mao H-K, Hemley RJ (1998) Brillouin scattering and X-ray diffraction of San Carlos olivine: direct pressure determination to 32 GPa. Earth Planet Sci Lett 279:11–19